Neutral tropical African CO$_2$ exchange estimated from aircraft and satellite observations

[1]Benjamin Gaubert, [2]Britton B. Stephens, [3]David F. Baker, [4,5]Sourish Basu, [6]Michael Bertolacci [7]Kevin W. Bowman, [1]Rebecca Buchholz, [7]Abhishek Chatterjee, [8]Frédéric Chevallier, [9]Róisín Commane, [6,7]Noel Cressie, [10]Feng Deng, [3]Nicole Jacobs, [11]Matthew S. Johnson, [12]Shamil S. Maksyutov, [13,14]Kathryn McKain, [7]Junjie Liu, [15]Zhiqiang Liu, [16]Eric Morgan, [3]Chris O'Dell, [17]Sajeev Philip, [18]Eric Ray, [7]David Schimel, [3]Andrew Schuh, [3]Thomas E. Taylor, [19,20]Brad Weir, [21]Dave van Wees, [22]Steven C. Wofsy, [6]Andrew Zammit-Mangion, [23]Ning Zeng

[1]Atmospheric Chemistry Observations & Modeling Laboratory (ACOM), National Center for Atmospheric Research, Boulder, CO, 80301
[2]Earth Observing Laboratory (EOL), National Center for Atmospheric Research, Boulder, CO, 80301
[3]cooperative Institute for Research in the Atmosphere, Colorado State University, Fort Collins, CO, USA
[4]Global Modeling and Assimilation Office, National Aeronautics and Space Administration, Goddard Space Flight Center, Greenbelt, MD 20771.
[5]Earth System Science Interdisciplinary Center, University of Maryland, College Park, MD 20740.
[6]School of Mathematics and Applied Statistics, University of Wollongong, Wollongong, Australia
[7]Jet Propulsion Laboratory, California Institute of Technology, Pasadena, CA, USA
[8]Laboratoire des Sciences du Climat et de L'Environnement, Institut Pierre-Simon Laplace, CEA-CNRS-UVSQ, Gif sur Yvette, 91191 CEDEX, France
[9]Dept of Earth & Environmental Sciences, Lamont-Doherty Earth Observatory, Columbia University, Palisades, NY 10964
[10]Department of Physics, University of Toronto, Toronto, Ontario, Canada
[11]Earth Science Division, NASA Ames Research Center, Moffett Field, CA, USA
[12]National Institute for Environmental Studies, Tsukuba, Japan
[13]Cooperative Institute for Research in Environmental Sciences, University of Colorado Boulder, Boulder, CO, 80309
[14]NOAA Global Monitoring Laboratory, Boulder, CO, 80309
[15]State Key Laboratory of Numerical Modeling for Atmospheric Sciences and Geophysical Fluid Dynamics, Institute of Atmospheric Physics, Chinese Academy of Sciences, Beijing, China
[16]Scripps Institution of Oceanography, University of California, San Diego, USA 92037
[17]Centre for Atmospheric Sciences, Indian Institute of Technology Delhi, New Delhi 110 016, India
[18]NOAA Chemical Sciences Laboratory, Boulder, CO, 80309
[19]Universities Space Research Association, Columbia, MD, USA
[20]NASA Goddard Space Flight Center, Greenbelt, MD, USA
[21]Faculty of Science, Vrije Universiteit, 1081HV Amsterdam, The Netherlands
[22]School of Engineering and Applied Science and Department of Earth and Planetary Sciences, Harvard University, Cambridge, MA, USA
[23]Dept. of Atmospheric and Oceanic Science and Earth System Science Interdisciplinary Center, University of Maryland, College Park, MD, USA

Plain Language Summary

Satellite CO$_2$ observations over land imply a major revision to our understanding of the global carbon cycle linked to large emissions from northern tropical Africa during the dry season, from October to May. We use aircraft observations made over the Atlantic Ocean in four seasons to evaluate flux models driven by a range of ground and satellite observations. Our results show that models using satellite observations over land overestimate annual emissions from northern tropical Africa by approximately 1 PgC yr^{-1}, concentrated in the dry season. At other times of year, satellite CO$_2$ observations provide improved estimates of northern tropical Africa exchange, with a stronger CO$_2$ uptake during the wet season.

Key Points:

- Emergent constraints derived from aircraft CO$_2$ measurements and inversions estimate a near neutral northern tropical African CO$_2$ budget.

- Inversions using satellite observations overestimate annual emissions from northern tropical Africa by approximately 1 PgC yr^{-1}.
- Satellite CO_2 observations imply a strong sink during the wet season over northern tropical Africa.

Corresponding author: Benjamin Gaubert, `gaubert@ucar.edu`

Abstract

Tropical lands play an important role in the global carbon cycle yet their contribution remains uncertain owing to sparse observations. Satellite observations of atmospheric carbon dioxide (CO_2) have greatly increased spatial coverage over tropical regions, providing the potential for improved estimates of terrestrial fluxes. Despite this advancement, the spread among satellite-based and in-situ atmospheric CO_2 flux inversions over northern tropical Africa (NTA), spanning 0-24°N, remains large. Satellite-based estimates of an annual source of 0.8-1.45 PgC yr^{-1} challenge our understanding of tropical and global carbon cycling. Here, we compare posterior mole fractions from the suite of inversions participating in the Orbiting Carbon Observatory 2 (OCO-2) Version 10 Model Intercomparison Project (v10 MIP) with independent in-situ airborne observations made over the tropical Atlantic Ocean by the NASA Atmospheric Tomography (ATom) mission during four seasons. We develop emergent constraints on tropical African CO_2 fluxes using flux-concentration relationships defined by the model suite. We find an annual flux of 0.14 ± 0.39 PgC yr^{-1} (mean and standard deviation) for NTA, 2016-2018. The satellite-based flux bias suggests a potential positive concentration bias in OCO-2 B10 and earlier version retrievals over land in NTA during the dry season. Nevertheless, the OCO-2 observations provide improved flux estimates relative to the in situ observing network at other times of year, indicating stronger uptake in NTA during the wet season than the in-situ inversion estimates.

1 Introduction

Tropical terrestrial ecosystems are an important component of the global carbon cycle as both a strong source of atmospheric CO_2 from land-use emissions (e.g., Hong et al., 2021) and a strong sink in intact forests, most likely owing to the CO_2 fertilization effect on photosynthesis (Lewis et al., 2009; Schimel et al., 2015). African ecosystems are large contributors to the uncertain positive climate-carbon cycle feedback of reduced photosynthesis and increased soil and plant respiration associated with hotter, drier conditions (Friedlingstein et al., 2006, 2010; Cox et al., 2013; Wang et al., 2014; Arora et al., 2020). Atmospheric inverse models constrained with in-situ observations estimate that the sum of land carbon fluxes from the tropics and southern extratropics has been near-neutral since the 2000s (Gaubert et al., 2019). The Global Carbon Budget 2021 (Friedlingstein et al., 2022) also estimates a near-balanced budget (excluding fossil fuel) in the tropics during the past decade that is derived from both process models and a set of atmospheric inversions.

CO_2 biomass burning emissions from sub-Saharan Africa show a marked seasonal cycle with large sources during the dry season, from October to May in the northern hemisphere (e.g., Roberts et al., 2009). Satellite observations from the NASA Orbiting Carbon Observatory-2 (OCO-2) indicate a strong and rapid increase in column CO_2 that coincides with the biomass burning season of northern hemispheric sub-Saharan Africa (Eldering et al., 2017; Crisp et al., 2022). Inversions of OCO-2 land nadir and land glint data (version B7.1) suggested that northern tropical Africa (NTA, 0-24 °N, Fig. 1) net biosphere exchange was a carbon source of approximately 1.5 PgC yr^{-1} to the atmosphere in 2015 and 2016 (Palmer et al., 2019; Crowell et al., 2019). OCO-2 land nadir and land glint inversions from version 9 of the OCO-2 Model Inter-comparison Project (v9 MIP, using version B9.1 OCO-2 data) also estimate a large source of carbon (1.26 ± 0.58 PgC yr^{-1}) over NTA, for the 4-year period of 2015-2019 (Peiro et al., 2022). This contrasts with the far less constrained in-situ set of v9 MIP inversion results for NTA, which provide a mean value of 0.23 ± 0.4 PgC yr^{-1}. Interannual variability in these in-situ inversions ranges between an NTA sink of 0.2 PgC yr^{-1} in 2018 and a source of 0.6 PgC yr^{-1} in 2016, during the 2015-2016 El Niño (Peiro et al., 2022).

In addition to the large uncertainties in the net budget, the component processes responsible for the large source indicated by OCO-2 observations have yet to be corroborated. Conceptually, net carbon exchange results from the the balance of varying gross fluxes,
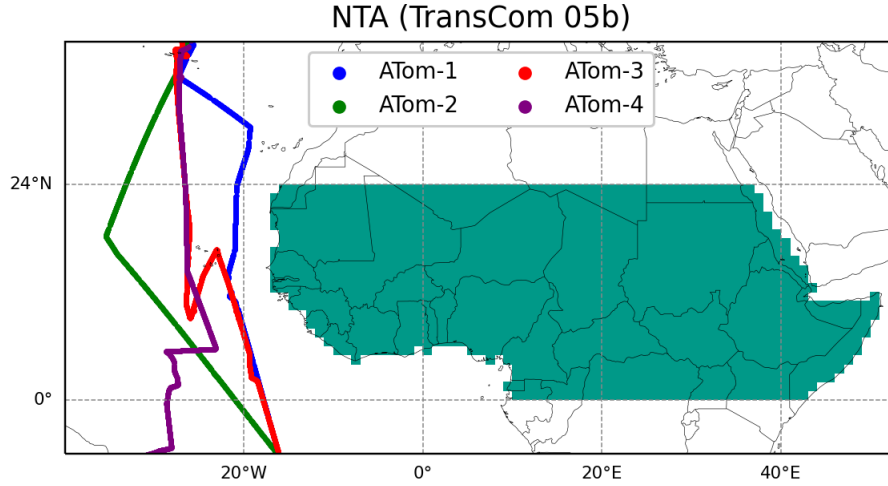
Figure 1. The TransCom 05b or northern tropical Africa (NTA) region. The NTA region encompasses various ecoregions including tropical forests, sub-humid savanna, semi-arid savanna, desert to semidesert, and shrubland areas. The four ATom flight tracks are also displayed.

including photosynthetic responses to drought, changes to plant and soil respiration, and direct effects of land use. Specific proposed mechanisms include soil emissions due to sustained land degradation (Palmer et al., 2019) and increased ecosystem respiration due to high surface temperature anomalies during the 2015-2016 El Niño (J. Liu et al., 2017). Another possibility is biases in the satellite measurements. Generating accurate OCO-2 CO_2 retrievals remains a challenge despite continuous improvements in the bias correction procedure (O'Dell et al., 2018). CO_2 retrieval biases can result from spectroscopic errors (Connor et al., 2008), aerosols and clouds over northern Africa (O'Dell et al., 2018; Nelson & O'Dell, 2019) and from surface pressure errors that are maximal over the tropics (Kiel et al., 2019). The empirically derived bias correction to OCO-2 data has an isolated maximum over NTA that is approximately +0.6 ppm higher than the global average. This is illustrated in Figure S1 and in Figure 4 of Taylor et al. (2023). Fires play an important role in the African carbon cycle, but are thought to be compensated by CO_2 uptake during the growing season (Valentini et al., 2014). The sub-Saharan region is dominated by shifting agriculture that is characterized by small and human-induced fires (Curtis et al., 2018). Emission estimates for this type of fire are uncertain and likely to be underestimated because global-scale fire emission models are typically based on satellite-derived burned area from relatively coarse-resolution sensors that are unable to detect most small fires (Randerson et al., 2012; Ichoku et al., 2016; Roteta et al., 2019; T. Liu et al., 2020). For 2016, a recent study (Ramo et al., 2021) used Sentinel-2 enhanced spatial resolution images to estimate burned area, and calculated for the African continent an increase of 31 % in fire carbon emissions compared to the Global Fire Emissions Database with small fires GFED4s (van der Werf et al., 2017). Estimates of annual-mean CO_2 emissions (Fig. S3) from fires range from 0.29 to 0.55 PgC/yr for 2016. Despite large uncertainties, an increase in 30 to 50 % in fire emissions does not suffice to explain the discrepancies in inversion results (Crowell et al., 2019; Palmer et al., 2019).

The atmospheric transport pathways exporting emissions from the African continent have been thoroughly studied by monitoring plumes over the Atlantic ocean using satellite remote sensing observations to track desert dust, smoke aerosols, and trace gases such as carbon monoxide (CO) (e.g., Prospero, 1999; Edwards et al., 2006; Adams et al., 2012; Barkley et al., 2019). Given the sparsity of other CO_2 observations downwind of tropical

Africa, the NASA airborne Atmospheric Tomography Mission (ATom) provides a unique opportunity to assess the ability of CO_2 inverse models to reproduce the atmospheric signatures of tropical African carbon fluxes over the Atlantic basin. The ATom campaign utilized the fully instrumented NASA DC-8 research aircraft to survey the chemical environment of the remote atmosphere around the world (Thompson et al., 2022). The ATom payload included three in situ CO_2 instruments and two whole air samplers with CO_2 measurements. ATom sampled vertical profiles along meridional transects of the Pacific and Atlantic Ocean basins (Fig. 1) during four month-long campaigns between August 2016 and May 2018.

In this study we use 54 OCO-2 v10 MIP inversions (Byrne et al., 2023) in the form of fourteen inverse models running five experiments assimilating different sets of observations. We apply an emergent-constraint approach (e.g., M. S. Williamson et al., 2021; Cox, 2019) in which we develop relationships between posterior CO_2 concentrations over the Atlantic and net biosphere fluxes from NTA (Fig. 1), and then use these to derive new flux estimates by comparison to the aircraft observations. The NTA region (TransCom 05b) is a subregion of the TransCom 05 region defined in the original TransCom experiment (Gurney et al., 2002; Gurney & Denning, 2008), spanning 0-24°N. The NTA region includes the Sahara desert and the CO_2 fluxes are primarily confined south of ∼18°N, across various ecoregions including tropical forests, sub-humid savanna, and semi-arid savanna.

2 Materials and Methods

2.1 OCO-2 v10 Model Intercomparison Project

The OCO-2 v10 Model Intercomparison Project (v10 MIP) consists of a large ensemble of atmospheric inversions from 14 modeling groups using primarily five combinations of in situ and OCO-2 satellite observations (Byrne et al., 2023). The models have different unoptimized prior flux distributions, model transport, and data assimilation techniques. Byrne et al. (2023) presented a description of the participating inverse models and of the assimilated datasets used in the OCO-2 v10 MIP. One notable difference to the preceding v9 MIP (Peiro et al., 2022) is that the OCO-2 v10 MIP uses OCO-2 observations over a longer time period and from a new XCO2 retrieval, i.e. the B10 version (Taylor et al., 2023) of the Atmospheric Carbon Observations from Space (ACOS) column-averaged dry air mole fraction of atmospheric CO_2 (XCO2) retrieval (Byrne et al., 2023; O'Dell et al., 2018; Kiel et al., 2019). The post-retrieval data processing also includes a quality filtering and a bias correction procedure (Kiel et al., 2019). The atmospheric inversions were conducted following a formal protocol with regard to the set of assimilated observations and their treatment. Five experiments were defined to investigate the impact of OCO-2 assimilation across viewing modes and to compare to the assimilation of baseline in-situ network observations. The experiments consist of: 1) in situ (IS), 2) OCO-2 land nadir and land glint (LNLG), 3) OCO-2 ocean glint (OG), 4) joint LNLG with IS (LNLGIS) and 5) a combination of all in situ and satellite data (LNLGOGIS). There were 12 participating inversion systems that provided outputs at the ATom locations, but not for all experiments for all of the simulations. We included the LoFI simulation in only the IS group. We include all of the available submissions when calculating an experiment average, which are 10 for LNLG, 11 for IS when including LoFI, and 11 for OG, LNLGIS, and LNLGOGIS.

2.2 Observations

We first merge the 10-second ATom dataset (Wofsy et al., 2021) and the ObsPack (Masarie et al., 2014) formatted posterior concentration files provided by the OCO-2 v10 MIP. Only airborne measurements along the northbound Atlantic transects were considered by selecting measurements made at longitudes between 70°W and 15°E. We excluded the last 15 min of the ATom-4 flight arriving in Recife, Brazil and the first 60 seconds of the flight departing to avoid local pollution influences. All of the data were then bin averaged on a 5° latitude by 50 hPa pressure grid. We define the metric ΔCO_2 (Eq. 1) by subtract-
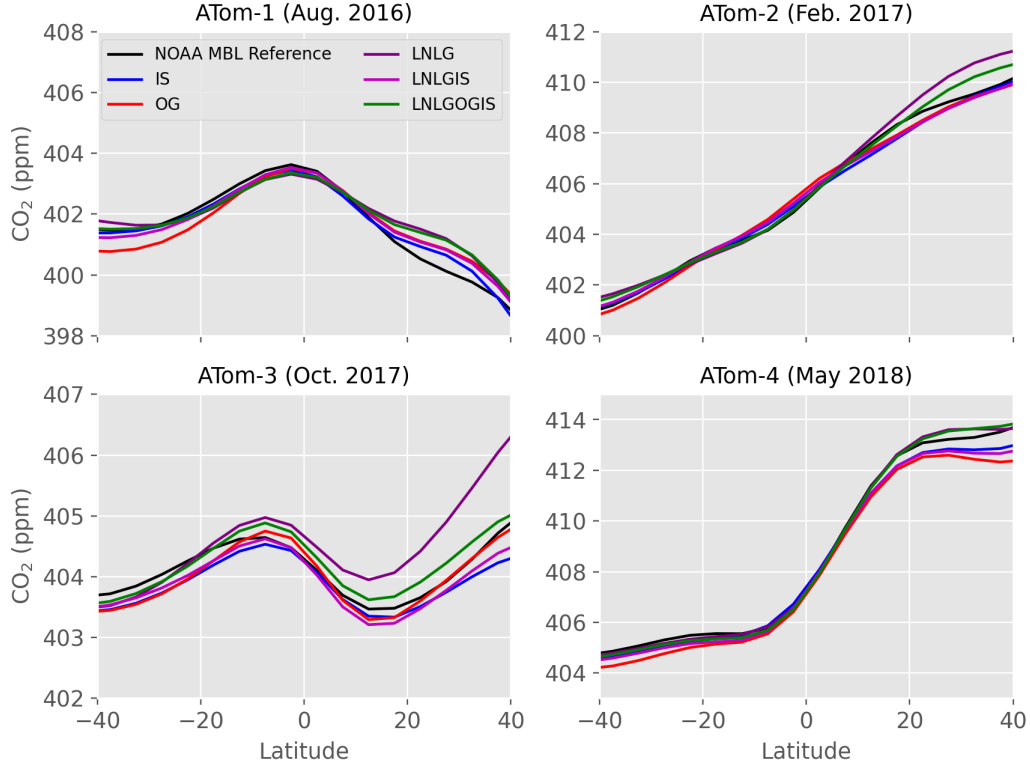
Figure 2. NOAA marine boundary layer reference CO_2 concentrations used to define ΔCO_2 for each ATom campaign. We also show the experiment average posterior marine boundary layer references estimated by the inversions. We use model-specific reference curves in the model posterior ΔCO_2 calculation.

Table 1. Optimized box boundaries (latitude in °N and pressure in hPa), flight dates intersecting boxes, correlation coefficients between the NTA fluxes and posterior ΔCO_2 in the corresponding box estimated by the v10 MIP ensemble, observed ΔCO_2 plus uncertainty, and estimated NTA flux plus uncertainty.

ATom	date	lat min/max	pressure max/min	r	Obs $\pm$ Unc. (ppm)	ATom-EC $\pm$ Unc. (PgC yr^{-1})
ATom-1	17 Aug. 2016	10/25	850/650	0.74	-0.65 $\pm$ 0.25	-2.81 $\pm$ 0.6
ATom-2	15 Feb. 2017	-5/10	950/500	0.77	1.9 $\pm$ 0.24	3.15 $\pm$ 0.6
ATom-3	17-20 Oct. 2017	-5/10	600/400	0.77	-1.11 $\pm$ 0.26	-2.22 $\pm$ 0.48
ATom-4	14 May 2018	-5/10	650/450	0.65	-0.71 $\pm$ 0.1	-0.26 $\pm$ 0.37

ing from the ATom observations and inversion posterior CO_2 the NOAA Greenhouse Gas Marine Boundary Layer (MBL) Reference surface (Dlugokencky et al., 2019) as defined by observations for ATom and as defined by the respective posterior CO_2 simulated at surface stations for the inversions.

$$\Delta CO_2 = CO_2^{\text{ATom}} - CO_2^{\text{MBL}} \tag{1}$$

The NOAA MBL reference product is derived from atmospheric CO_2 mole fraction measurements from the NOAA ESRL Carbon Cycle Cooperative Global Air Sampling Network (Dlugokencky et al., 2019). In order to generate a consistent MBL reference for both the model and observations, we ran the Python version of the curve fitting and smoothing algorithm developed by Thoning et al. (1989) over the period 2015–2020 using the subset of stations available during this time. We linearly interpolate the MBL reference values to our 5° latitude bins. We use the weekly values that are closest in time to the ATom measurements, 16 August 2016 (ATom-1), 15 February 2017 (ATom-2), 16 October 2017 (ATom-3), and 17 May 2018 (ATom-4). Figure 2 shows the selected MBL reference values used to define ΔCO_2 for the observations and as averaged for each experiment. The experiment mean posterior MBL gradients diverge up to 1 ppm from the observations. Thus, subtracting reference values specific to each model and experiment is an important step to isolate NTA signals from those originating elsewhere.

2.3 Averaging box selection

We identified optimal pressure and latitude bounded boxes by maximizing the across-inversion correlation coefficient between ΔCO_2 averaged over a given ATom box and fluxes for the same month from the NTA TransCom region. This results in a correlation calculation across 54 data pairs. Note that the ATom Atlantic flights all generally occurred in the middle of the month (Table 1) leading to our use of monthly mean fluxes. Also, back trajectories indicate that NTA had a strong influence on the measurements over the preceding several weeks (Fig. 3). We imposed that the boxes have a minimum width of 15° in latitude and a minimum height of 200 hPa, to avoid spurious correlations. We then calculated correlation coefficients for all different possible configurations spanning 40°S to 40°N in latitude and from the surface to 200 hPa. While significant relationships (with p-value lower than 0.05) are found for many different boundary options (Fig. S4), we select the box that provides the greatest correlation coefficient (Table 1). Given transport differences across models, we interpret these regions as having the greatest agreement across models as to where NTA fluxes influence the observed concentrations. Table 1 includes the boundaries of the optimized boxes and the Pearson correlation coefficient between the posterior ΔCO_2 box average and the respective TransCom subregion monthly net land fluxes.

2.4 Observation uncertainty

We use CO_2 measurements made by three in-situ analyzers: the NOAA Picarro instrument, the Harvard quantum cascade laser spectrometer (QCLS, Santoni et al., 2014), and
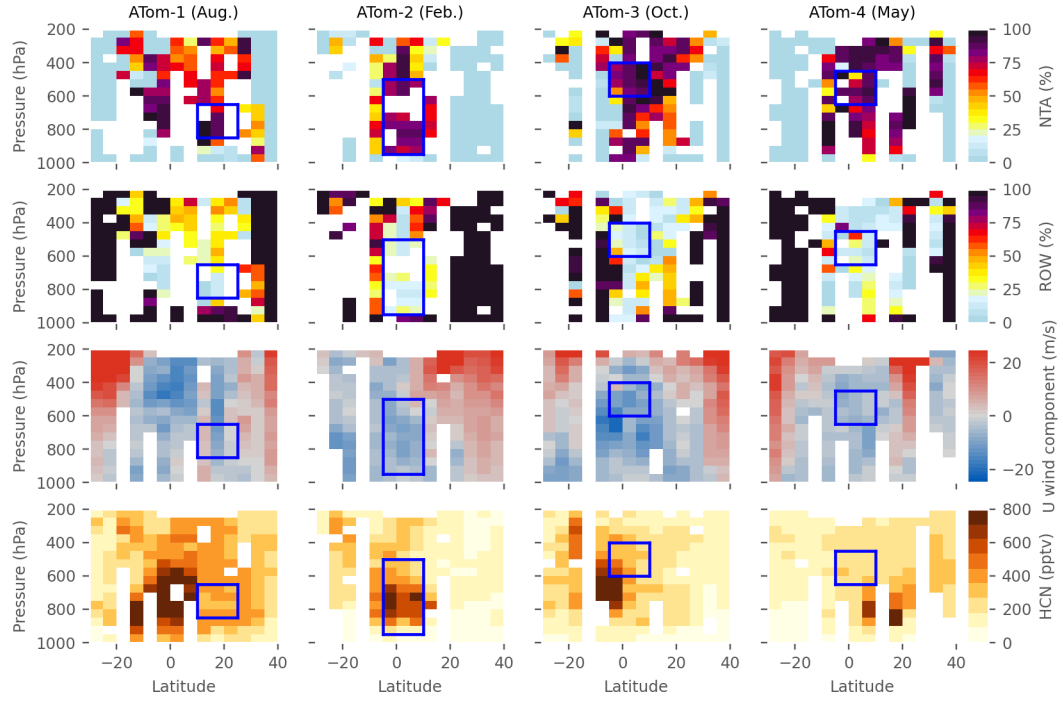
Figure 3. Relative contributions from the the NTA region (first row) and the rest of world (second row) to the Atlantic ATom observations, based on 14-day back-trajectories. Distribution of the U zonal wind speed (third row) and HCN (fourth row) over the Atlantic for all four ATom campaigns. In these plots solid blue lines show the optimized boxes. Bins containing no flight data are white.

the National Center for Atmospheric Research (NCAR) airborne oxygen instrument (AO2, Stephens et al., 2021). We also use CO_2 measured in flasks collected by the NCAR/Scripps Medusa whole-air sampler (Stephens et al., 2021) and NOAA Programmable Flask Packages (PFP) (Sweeney et al., 2015). The ΔCO_2 values used in the emergent constraint have been calculated using the NOAA Picarro data as it is most closely tied to the WMO CO_2 scale, has the greatest data coverage, and is the record the models used for reporting matched posterior concentrations. To assess uncertainty in these observations, we compare ΔCO_2 estimates among all five in-situ measurement or sampling systems. More specifically, to allow for different periods of missing data for each instrument owing to in-flight calibrations and the reduced coverage of the flask systems, we first calculate sensor-sensor differences using the NOAA Picarro data as the common reference and then calculate box averages of these differences. We then use the standard deviation of these four differences, also including zero for the NOAA Picarro minus itself, as the observational uncertainty on box-averaged ΔCO_2 for each campaign (Table 1).

2.5 Emergent constraints

We use weighted orthogonal distance regression (Boggs & Rogers, 1990), a method which accounts for errors in both the explanatory and response variables, to construct emergent constraints between ΔCO_2 (here the explanatory variable) and NTA flux (here the response variable). Weighted ODR requires knowledge of the variances of the errors associated with each variable. As scaling factor for the flux errors we use the empirical standard deviation of the flux estimates, while for the ΔCO_2 errors we use the empirical standard deviation of the ΔCO_2 values. The linear fit and its associated coefficient uncertainty depend only on the ratio of these scaling factors, so we are implicitly assuming that the signal to noise ratio (defined as the variance of the data divided by the variance of the associated errors) of the fluxes is the same as that of ΔCO_2. In the absence of more information about the sources of variation in the errors, this is a reasonable assumption.

Recent comparisons of different statistical methods for estimating emergent constraints found broadly consistent results (Renoult et al., 2020; Simpson et al., 2021). The emergent constraints developed here are based on an ensemble with overall good structural diversity, thanks to the assimilation of various kinds of observations and using a range of transport models. Also, there are no attempts to quantify a range of projected responses from our ensemble, which can be a problem when assessing Earth system response to a forcing or the strength of a feedback (Sanderson et al., 2021). However, it remains important to accurately quantify uncertainties (e.g., K. W. Bowman et al., 2018; D. B. Williamson & Sansom, 2019).

We account for uncertainties in both ATom observations and the MIP results through the following. First, we draw a sample of the regression line using the error covariance matrix of the estimated regression parameters, as well as a sample from the ATom ΔCO_2 observation error distribution (as derived in the previous section). Second, we find the corresponding flux estimate using this sampled regression line and the sampled ATom ΔCO_2 measurement. Third, a sample from the flux error distribution assumed by the ODR method is added onto this flux estimate; this is assumed to be a normal distribution with mean zero and variance equal to the empirical variance of the residuals from the ODR fit. We repeat this process 5000 times and then take the empirical standard deviation of the flux samples as the 1σ uncertainty of the ATom-EC flux. This method accounts for uncertainty associated with the emergent constraint fit and the ATom CO_2 measurement uncertainty, but not for the uncertainty arising from the choice of the altitude-latitude box; we discuss this form of uncertainty in Section 3.3.2 and in the supplementary material. The resulting four monthly ATom-EC values with their uncertainties are reported in Table 1.
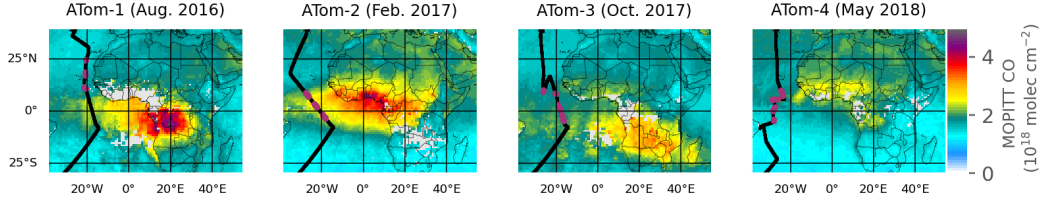
Figure 4. Terra/MOPITT V9J level 3 monthly average total column of carbon monoxide for months corresponding to the ATom campaigns, and ATom flight tracks. The ATom observations in purple correspond to the optimize boxes.

2.6 Source Contributions and Ancillary Measurements

For qualitative assessment of sampled air origins, backward particle trajectories were computed using the Traj3D model (K. P. Bowman, 1993; K. P. Bowman & Carrie, 2002). Model trajectories were initialized at receptors spaced 1 min apart along the ATom flight tracks, and followed backwards for 30 d (Ray, 2022; Gonzalez et al., 2021). From these trajectories, we calculated for each receptor point the surface influence functions over land only. These footprints (Fig. S5) are in units of concentration mole fraction per emission flux or ppm/(μmol m^{-2} s^{-1}). We define the relative contribution of the NTA TransCom subregion and the rest of the world (ROW) to the ATom tropical Atlantic measurements. The footprints, either for NTA or ROW, are summed and divided by the global total footprints. We show the contributions for 14-day back trajectories for each 5° latitude by 50 hPa pressure grid bin (Fig. 3). The regions of strong NTA influence are large for all ATom missions. While these back trajectories were not used in the determination of the boxes, there is a good correspondence with a majority of the air in our optimized boxes strongly influenced by fluxes from the NTA TransCom subregion (Figs. 3, S4).

Fig. 3 shows two additional ATom measurements, the eastward (U) wind speed component and hydrogen cyanide (HCN) concentration measured by the Chemical Ionization Mass Spectrometer (CIT-CIMS) instrument. HCN is an excellent biomass burning tracer (Li et al., 2003; Crounse et al., 2009).

Fig. 3 also shows the optimized boxes. We also show on Fig. 4 maps of the the monthly mean CO total column from the V9J MOPITT product (Deeter et al., 2022). The biomass burning plumes characterized by enhanced CO column and in-situ HCN can clearly be identified. These features correspond to plumes from NTA on ATom-2 and ATom-4, and from southern tropical Africa on ATom-1 and ATom-3.

3 Results

3.1 NASA ATom Concentrations

The four ATom campaigns observed both elevated and depleted CO_2 over the tropical Atlantic relative to the NOAA Marine Boundary Layer (MBL, Fig. 2) Reference (Dlugokencky et al., 2019). We define a metric quantifying these anomalies, ΔCO_2, by subtracting the NOAA MBL Reference at corresponding latitudes and times from the ATom CO_2 observations (Fig. 5). We qualitatively attribute these CO_2 variations to biomass burning or net ecosystem exchange in tropical Africa guided by observed winds, modeled
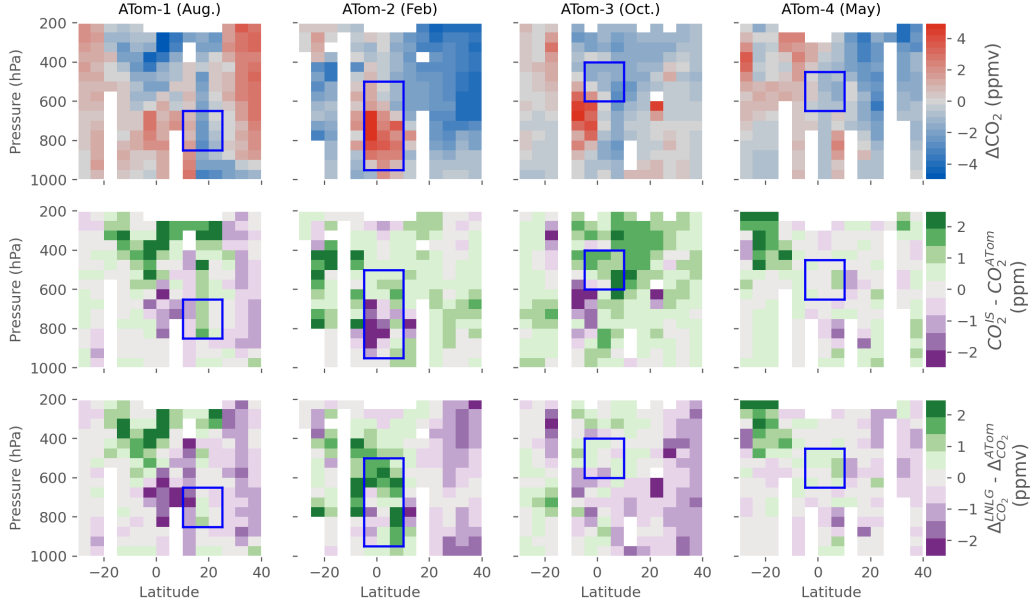
Figure 5. Latitude and altitude distribution of ΔCO_2 observations made over the Atlantic basin for the four ATom deployments. ΔCO_2 is defined by subtracting the observed or modeled NOAA MBL Reference (Dlugokencky et al., 2019) at corresponding latitudes and times from the ATom CO_2 observations or inverse models, respectively. The second and third rows show the IS and LNLG experiment mean bias, respectively. The optimized NTA-influenced boxes are delineating by solid blue lines. Bins containing no flight data are white.

back-trajectories, satellite CO observations, and coincident in situ measurements of biomass burning tracers (Fig. 3, 4).

The ATom-1 deployment occurred in August 2016. Typically at this time of year, the western African monsoon brings rain over western Africa, inducing a convection-driven upward and westward atmospheric pattern, which is strongest near the Inter-Tropical Convergence Zone (ITCZ) (Rodríguez et al., 2015). As a result of the NTA growing season CO_2 uptake, ATom-1 observed negative ΔCO_2 throughout the troposphere north of 15°N and more broadly in the upper troposphere (Fig. 5). The mean values from the IS experiment tends to overestimate ΔCO_2 in these negative CO_2 anomaly regions, suggesting an underestimated uptake.

ATom-2 occured in February 2017 during the NTA dry season and sampled biomass burning plumes from the region (Figs. 3, 5). During ATom-2, large positive ΔCO_2 values were found centered around the equator, between 950 hPa and 500 hPa. The LNLG experiment mean strongly overestimates ΔCO_2 within and adjacent to this observed positive anomaly, whereas the IS experiment mean slightly underestimates concentrations in the plume.

ATom-3 occured in October 2017 during the NTA wet-to-dry transition season. The negative ΔCO_2 values during ATom-3, located north of the Equator, between 600 and 400 hPa in the mid-troposphere, appear to originate from eastern NTA (Fig. S5). South of the Equator between 600 and 800 hPa ATom-3 intercepted a biomass burning plume that originated from southern tropical Africa (Fig. 3). The IS mean experiment strongly underestimates ΔCO_2 in this biomass burning plume, but overestimates ΔCO_2 in the negative

anomaly regions. The LNLG experiment mean performs better for both positive and negative anomalies during ATom-3.

ATom-4 measurements were made in May 2018 during the dry-to-wet transition season for NTA. Negative ΔCO_2 values can be found over the optimized box between -5°N and 10°N and 450-650 hPa. It is located just above a region of positive ΔCO_2 values that correlate with elevated HCN in the ATom data (Fig. 3). This enhancement in ΔCO_2 is slightly underestimated by both the IS and LNLG inversion means.

3.2 Emergent Constraints

Emergent constraints are powerful tools to reduce model spread and narrow uncertainty (e.g., K. W. Bowman et al., 2018; Eyring et al., 2019; M. S. Williamson et al., 2021; Simpson et al., 2021). They offer a promising way to further improve the quantification of carbon fluxes and the overall scientific understanding of the carbon cycle (e.g., Stephens et al., 2007; Cox, 2019; Keenan et al., 2021; Long et al., 2021; Barkhordarian et al., 2021). Overall, our approach here is to take advantage of the large model spread to derive robust relationships between the airborne observations and land fluxes. We utilize CO_2 gradients (ΔCO_2) observed during ATom as a measurable variable (predictor) to obtain a constrained estimate of net land fluxes from NTA. For each ATom deployment, we use the v10 MIP ensemble to determine an altitude-latitude box boundary within the airborne transects that best correlates with NTA fluxes (Fig. 5). We also tried defining boxes centered on the observed biomass burning plumes and on the basis of back-trajectories (Fig. 3). The former only captured strong positive emissions while ignoring uptake signals, and the latter showed worse correlations most likely owing to differences in transport between the back-trajectory model and the inversions. Thus we chose to optimize the boxes based on empirical correlations, which to some extent can allow for differences among the transport models by expanding the boxes. We calculated the Pearson correlation coefficient between model ΔCO_2 and NTA fluxes The optimized Pearson correlation coefficients range from r=0.65 for ATom-4 to r=0.77 for ATom-2. We consider the true relationship to be unknown and we expect scatter of the v10 MIP points about the true relationship because of transport differences and other sources of errors between inversions. We also do not expect the correlations to reach one because of variations in contributions to CO_2 within the boxes from regions other than NTA.

Fig. 6 shows the relationships between the NTA land fluxes (excluding fossil fuel emissions) and ΔCO_2 averaged over the respective ATom box (Table 1, Fig. 5). We use these emergent relationships to estimate NTA fluxes for all four ATom periods. The fit slopes in Fig. 6 represent the sensitivity of concentrations to fluxes, as defined by this v10 MIP collection of models. We plot the dependent concentration variable on the x-axis to be consistent with the emergent constraint predictor convention. We estimate fluxes in the months corresponding to each campaign as the intersection of the observation and fit lines shown in Fig. 6. We estimate the observation error by comparing the five different CO_2 observing systems aboard the DC-8, three in situ and two flask samplers. We estimate 1σ flux uncertainty by propagating the observation error onto the fit prediction interval (see Section 2).

ATom-2 was characterized by a strong source as measured by a ΔCO_2 of around 2 ppm (Table 1). Yet, the LNLG and LNLGIS experiments show a strong overestimation of this signal, with almost all inversions simulating a ΔCO_2 higher than observations. The IS models exhibit the largest spread of all experiments, but generally show a positive bias during ATom-1 and ATom-3 during the wet season and wet-to-dry season transition and a negative bias during ATom-4 during the dry season. During ATom-3, the IS group overestimates ΔCO_2 with biases up to 2 ppm. Even though ATom-3 occurred at the end of the wet season, some inversions indicate a land source of CO_2 for NTA at this time. There was no clear ranking for inversion performance between experiments as their skills were not
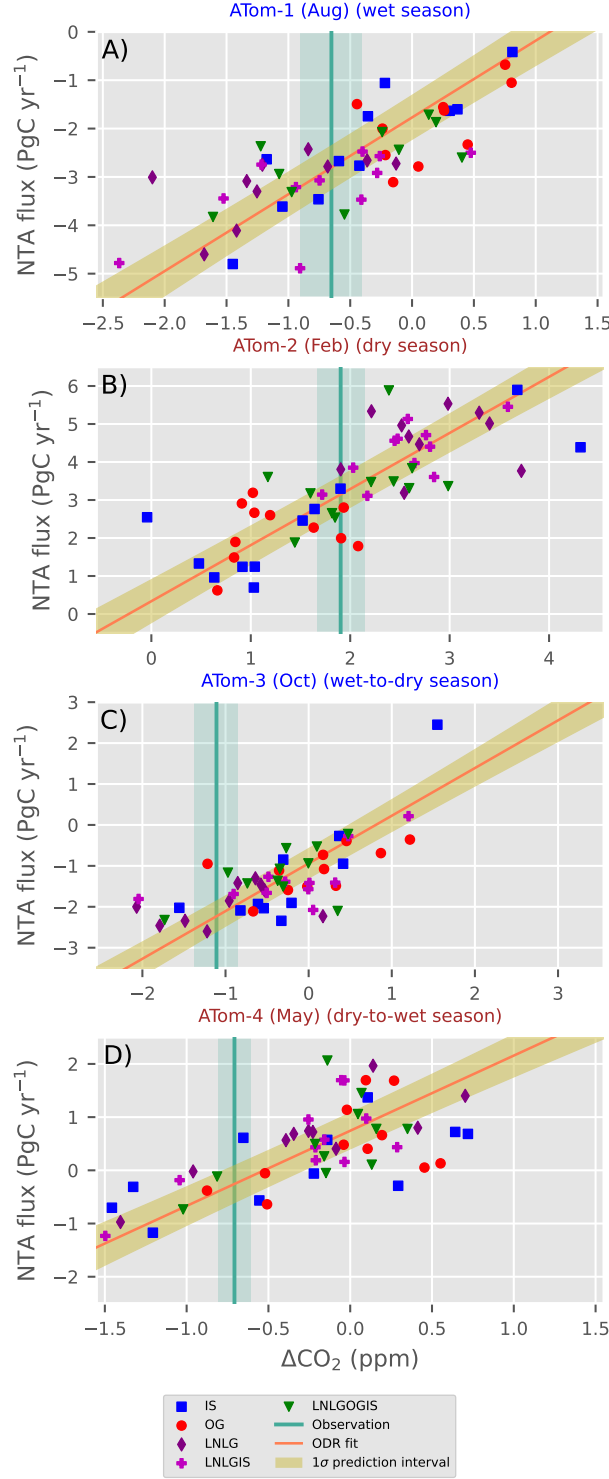
Figure 6. Emergent constraints on northern tropical African CO_2 fluxes during ATom. The relationships represent the sensitivity of airborne posterior ΔCO_2 to NTA land fluxes (excluding fossil fuel emissions). Each point shows results for a single model within one of four experiments (colors). Fluxes are averaged over the month of each campaign and the NTA TransCom subregion. The ODR fits are plotted as an orange line with a brown shading indicating 1σ prediction intervals. The vertical line in each panel represents the observed ΔCO_2, averaged over the optimized boxes shown in Fig. 5. Shading around the observation lines represents 1σ observation uncertainty (2). Note the different axis ranges between panels. The same figure with simulations colored by inverse models can be found in the supplement (Fig. S6).
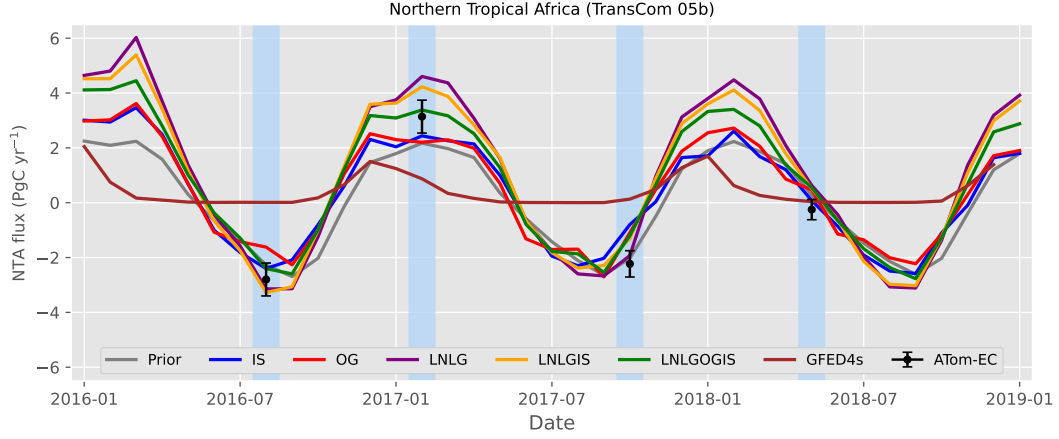
Figure 7. Monthly mean northern tropical Africa net land CO_2 fluxes for the different OCO-2 MIP experiments compared to the observational estimates. Lines represent means across all models within each experiment. The ATom emergent constraint (ATom-EC) is plotted in black with each 1σ prediction interval as an errorbar. We also show the mean prior fluxes used in the inversions and biomass burning fluxes from GFED4s (v4.1) (van der Werf et al., 2017), used as prior fire fluxes by 3 out of 12 inversion models.

consistent across the four campaigns (Fig. 6). Although we present experiment means in Fig. 7 for visual clarity, Fig. 6 suggests that experiment means do not necessarily reflect best estimates. It is also not clear that any particular models perform better or worse than others across all four campaigns. Thus, we do not evaluate individual models, but do provide a version of Fig. 6 colored by model in the supplement (Fig. S6).

3.3 Northern Tropical African Land Fluxes

3.3.1 Monthly Time Series

Figure 7 shows the monthly average land fluxes averaged for each experiment, from 2016 to 2018, along with our ATom emergent constraint (hereafter ATom-EC) estimates for the four ATom missions. The ATom-1 emergent constraint suggests a strong wet-season land sink that is more closely reproduced with the inversions that assimilate OCO-2 LNLG data. During ATom-2, which occurred during the dry season, all the experiments indicate a larger source than was predicted by the prior fluxes. The spread between experiments is also maximal for ATom-2, with the LNLG and LNLGIS mean overestimating the ATom-EC and IS and OG slightly underestimating. The LNLGOGIS mean is closest to our ATom-2 estimate as it combines the LNLG overestimation and the IS/OG underestimation, as shown on Fig. 6b. The IS flux mean underestimates the magnitude of the seasonal cycle as it is positively biased during ATom 1 and 3 and negatively biased during ATom 2 and 4. During the shoulder seasons, the spread among the four experiment means is smaller and the OCO-2 LNLG based inversion mean is in agreement with the ATom-EC for ATom-3 in showing a much lower flux. Our results indicate that the assimilation of OCO-2 data improves the inversions for ATom-1 and ATom-3.

These campaign differences are related to seasonal patterns evident in the multi-year monthly-mean fluxes. On average, the inversions that assimilate OCO-2 land data (LNLG, LNLGIS, LNLGOGIS) have a stronger source during the dry season (Figure S7). The LNLG and LNLGIS fluxes are higher than the other experiments from January to May. However, the LNLG and LNLGIS inversion fluxes are more negative than the IS fluxes in the wet
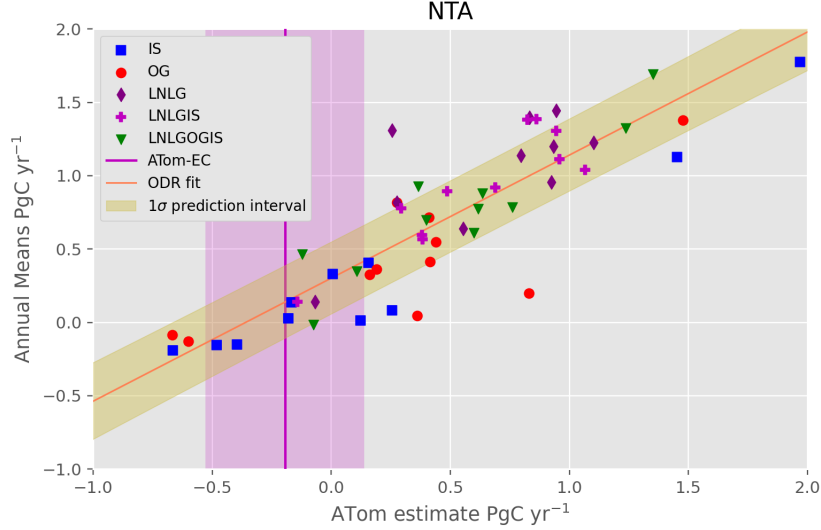
Figure 8. NTA three-year mean emergent constraint: True modeled three-year means (2016-2018) versus estimates based on model flux estimates corresponding to the four ATom campaigns. The fit represents the correction of the ATom-based estimates to the true three-year means (2016-2018) for temporal sampling biases. The ODR fit is plotted as an orange line with shading indicating the 1σ prediction interval. The vertical line represents the ATom-derived preliminary three-year mean flux estimate. Shading around the observation line represents the 1σ ATom-EC mean flux uncertainty.

season, from August to October. As a result, all the experiments using OCO-2 land data have a stronger seasonal cycle than the IS experiment. This is in line with a recent study that found a stronger seasonal amplitude when comparing the OCO-2 LNLG inversions with the IS inversion over South Asia (Philip et al., 2022). The OG experiment fluxes are close to those of the IS experiment, but in 2018 higher than IS during the dry season. With no data constraints over NTA, the IS and OG inversions remain close to the prior estimates. It is important to note that for OG the land flux is estimated by data over the ocean only and also that potential biases in OG observations may impact the posterior fluxes (Crowell et al., 2019; Peiro et al., 2022).

3.3.2 2016-2018 Mean Flux Estimates

We derive an initial multi-year annual mean NTA flux estimate by scaling the inversion average climatological seasonal flux cycle to optimally fit the four ATom-EC flux estimates (2016-2018). We fit the 4 ATom estimates to the average seasonal cycle derived from all the inversions. We input the 1σ uncertainty described above to account for uncertainties in each ATom. To account for the assumption of a specified seasonal cycle shape, we repeat the fit using all the individual modelled seasonal cycles and add the standard deviation in quadrature to the fit error.

The optimally scaled seasonal cycle represents a preliminary three-year annual mean flux estimate subject to potential seasonal and interannual sampling biases owing to the flights occurring at only select times of year and in select years. To correct for this, we use the inversion suite to estimate the difference between the annual mean estimated in this way from the four ATom-EC and the true three year mean from each inversion. This approach relies on the inversions, as internally consistent representations of seasonally and interannually
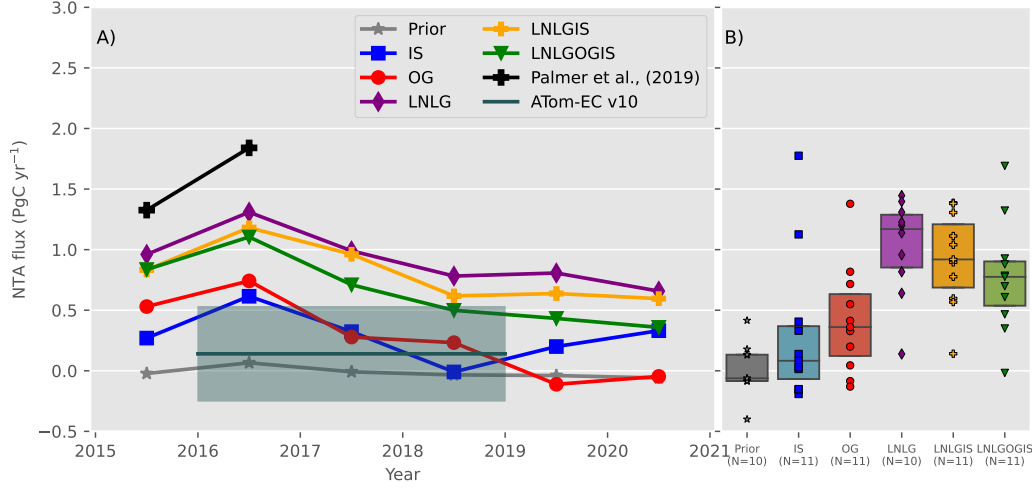
Figure 9. A) Annual mean net land CO_2 fluxes for NTA averaged for each MIP experiment and from the airborne observational constraint. The ATom emergent constraint (ATom-EC) is plotted in cyan with a shaded 1σ error estimate. We also show the mean of five inversions for 2015 and four inversions for 2016 from Palmer et al. (2019). B) 2016-2018 means for each inverse simulation (dots), and the resulting boxplot (25th percentile, median and 75th percentile) by experiment, and also showing priors.

varying fluxes and concentrations, to predict our temporal sampling biases in estimating three-year mean fluxes. We first calculate three-year mean fluxes for each inversion using a linear fit of the average seasonal cycle to the four monthly fluxes corresponding to the ATom months. We then compare these to the true mean fluxes (2016-2018) from each inversion. Because the inversions suggest both an offset and slope component to this correction (Fig. 8), we again use an emergent constraint approach to define the correction and its uncertainty. We calculate the relationship between the true three-year annual means and the 4-ATom estimate using the same method as for the individual campaign estimates, an ODR fit with input uncertainties scaled according to the respective standard deviations (Fig. 8). We estimate a slope of 0.84 PgC yr^{-1} per PgC yr^{-1} with an intercept of 0.3 PgC yr^{-1}, and a correlation coefficient of 0.87. We calculate the corrected ATom-EC 2016-2018 mean estimate and its 1σ uncertainty by propagating the uncertainty errors using the same three step Monte-Carlo approach described in the previous section, using as inputs each ATom-EC and its 1σ uncertainty for the observation.

We obtain a corrected three-year annual mean flux estimate of 0.14 PgC yr^{-1} with a 1σ uncertainty of 0.39 PgC yr^{-1} (Fig. 9). It is important to note that this estimate and its relatively small uncertainty come not just from the four ATom transects spread over three years but rather a combination of these transects and estimates of the underlying seasonal and interannual variations from the suite of 54 models.

Although for differing time periods, our estimate contrasts with the findings of Palmer et al. (Palmer et al., 2019) for 2015-16, based on the assimilation of land Atmospheric Carbon Observations from Space (ACOS) v7.1 retrievals of GOSAT (Greenhouse Gas Observing Satellite) and OCO-2, and of the v9 MIP LNLG experiment for 2015-2018 (Peiro et al., 2022) that are on average 1.6 and 1.25 PgC yr^{-1}, respectively. For the v10 MIP, the mean NTA fluxes for the same 2016-18 period are 1.03 ± 0.38 PgC yr^{-1} for the LNLG experiment.

The NTA fluxes for the v10 MIP IS and OG experiments are much weaker with 2016-2018 means of 0.31 and 0.42 PgC yr^{-1}, respectively. All the v10 MIP experiments are

consistent in showing an enhanced 2016 source, likely due to the 2015-2016 El Niño, and a $\sim$0.5 PgC yr^{-1} reduction of the source between 2016 and 2018 (Fig. 9). The LNLGOGIS range (1.71 PgC yr^{-1}) and that of IS (1.96 PgC yr^{-1}) are larger than other experiments (Fig. 9).

To evaluate the impact of the choice of a single box to determine the emergent constraints, we repeated the entire annual-mean calculation with alternate altitude-latitude boundaries for the boxes. We varied one box at a time among the 12 highest correlated boxes for each ATom and calculated all different possibilities for 10^4 realizations. The resulting distribution of annual mean estimates is a normal distribution with a median and mean that are both equal to the the mean estimate using only our optimal four-box ATom-EC estimate. We add the standard deviation of this distribution, 0.1 PgC yr^{-1}, in quadrature with our uncertainty as an estimate of errors in the choice of box boundaries, resulting in a final uncertainty of $\pm$ 0.39 PgC yr^{-1}.

4 Discussion

Previous studies estimated a near neutral African CO_2 budget with photosynthesis being larger than the sum of respiration, biomass burning and fossil fuel emissions combined (Ciais et al., 2009; Valentini et al., 2014). The net biospheric carbon uptake is suggested to mainly occur in intact forests (Ciais et al., 2009; Lewis et al., 2009), as estimated by vegetation models and forest inventory plots. The long-term inventory plots of the African Tropical Rainforest Observatory Network, or AfriTRON, remained a live biomass carbon sink despite extreme environmental conditions during the 2015-2016 El Niño event (Bennett et al., 2021). This implies a strong uptake in intact, old-growth, tropical forests in line with above-ground carbon storage estimates (Pan et al., 2011). However, the 2015-2016 El Niño (J. Liu et al., 2017) may have had long lasting impact with a slow recovery in forest uptake. There may be other sources of CO_2 from unaccounted deforestation and degradation (Wigneron et al., 2020).

Global CO_2 inverse models rely on prior fluxes provided for example from model products, such as biosphere models (Philip et al., 2019) and are subject to large-scale transport uncertainty, given their coarse horizontal and vertical resolutions (e.g., Schuh et al., 2019). Knowing the importance of transport errors through diffusive and convective vertical mixing in explaining the systematic differences between TM5 and GEOS-chem (Schuh et al., 2019, 2022), we repeated our emergent constraint approach using only the subset of 3 TM5 (TM5-4DVAR, OU and CT) or the 5 GEOS-Chem (Ames, CMS-Flux, COLA, UT and WOMBAT) inversions (Fig. S6). A previous study on CO showed that we also expect the differences to be maximal in outflow pathways of large biomass burning sources (Ott et al., 2011). We found a three-year annual mean flux estimate of 0.27 $\pm$ 0.36 (TM5) and 0.8 $\pm$ 0.43 (GEOS-Chem) PgC yr^{-1}. These uncertainty estimates do not reflect the bias imposed by the choice of a single transport model. This reinforces the need for emergent constraints using relationships derived by a diverse suite of models.

In addition, inversion algorithms are sensitive to the observations' spatial coverage and temporal frequency, and with particular relevance for satellite CO_2 observations also to measurement biases (e.g., Basu et al., 2018; Houweling et al., 2015). Inversion of SCIAMACHY (Kaminski et al., 2017), GOSAT and OCO-2 CO_2 retrievals over land suggest a source in the tropics, driven by NTA region emissions (Houweling et al., 2015; Palmer et al., 2019; Crowell et al., 2019; Peiro et al., 2022). Mean estimates from previous GOSAT and OCO-2 studies range between 1.25-1.6 PgC yr^{-1}. The magnitude of these unexpected sources equates to approximately half of the global net land carbon sink (Friedlingstein et al., 2022) and would require a major revision to our understanding of both the tropical and global carbon cycle. A large NTA source has not been seen in the most recent IS inverse model synthesis studies (Crowell et al., 2019; Gaubert et al., 2019; Peiro et al., 2022). Overall the larger CO_2 land source estimates are driven by satellite retrievals during the dry season (Fig. 7), when there

is a high aerosol loading from biomass burning and dust which may increase biases (Fig. S1) in retrievals (O'Dell et al., 2018). The lack of ground-based observations over Africa makes it challenging to verify these estimates. Thus, airborne measurements such as those from ATom are uniquely valuable in assessing the divergent inversion estimates. During ATom-2, the ATom-EC indicates a smaller source of 3.15 ± 0.6 PgC yr^{-1} (mean $\pm$ 1σ uncertainty, Fig. 7) in February than the LNLG experiment with 4.6 ± 0.74 PgC yr^{-1} (mean $\pm$ 1σ across 10 models).

It is possible that remaining biases in version B10 OCO-2 measurements over NTA led to erroneous flux estimates in inversions using these data. NTA during the dry season exhibits very high dust and smoke aerosol loading (Fig. S1d), associated with Harmattan winds (Evan et al., 2006). The OCO-2 retrievals undergo quality filtering based on multiple parameters, including aerosol optical depth (O'Dell et al., 2018), and for NTA during dry season typically less than 10 % of retrievals pass this filter (Fig. S1b). The OCO-2 retrievals also have a multi-parameter post-retrieval empirical bias correction applied (O'Dell et al., 2018), and this bias correction is largest over NTA, with adjustments of approximately $+2.7$ ppm, or 0.6 ppm higher than the global average correction (Fig. S1a). This large bias correction is tied primarily to two terms, one encompassing dust, water, and sea-salt aerosol loading and a second related to the difference between retrieved surface pressure and that from meteorological reanalyses, which itself may result from aerosols (Kiel et al., 2019).

The positive dry season OCO-2 bias correction over NTA would have to be overestimated if it were to explain the sign of the LNLG inversion versus ATom-EC differences we see. How large of an overestimate might be required to explain our result? Given the many interacting constraints in global CO_2 inversions, and uncertain atmospheric transport, it is difficult to quantitatively estimate the magnitude of biases necessary. For example, the LNLG mean concentration bias in the ATom-2 optimized box is 0.88 ppm. However, we expect flux signals to be more concentrated in these optimized boxes than in full column XCO2 measurements because they only represent partial columns, but also less concentrated because of lateral and vertical mixing between NTA and the mid-Atlantic. Previous synthetic inversion work has demonstrated a high sensitivity of continental scale inverse flux estimates to small biases in satellite XCO2 measurements, on the order of 1 PgC yr^{-1} per ppm (Chevallier et al., 2007). We find a correlation between the dry season XCO2 over NTA in posterior concentration fields and NTA fluxes from the inversions with a slope of 4.16 PgC yr^{-1} per ppm or 1.39 PgC/ppm for 4 months (DJFM) (Fig. S2). This implies that the disagreement we find between the 1.03 PgC yr^{-1} LNLG inversion experiment mean and our ATom-EC estimate of 0.14 PgC yr^{-1} might potentially be explained by a $+0.64$ ppm bias concentrated in Dec-Mar or just a $+0.21$ ppm bias if it persists throughout the year.

Despite the apparent overestimated source in the LNLG experiment, our ATom-EC estimate for ATom-2 still shows a stronger NTA source than in previous and v10 MIP IS inversions. Biomass burning emissions could play a role in the enhanced source, but need improved observational constraints. Recent studies have found that the dry matter burned estimates and the number of active fire detections over Africa could be underestimated by the 500-m resolution MODerate resolution Imaging Spectroradiometer (MODIS) instrument (Ichoku et al., 2016; Roteta et al., 2019; Nguyen & Wooster, 2020). The detection and inclusion of smaller fires detected by the higher-resolution 20-m Sentinel-2 Multispectral Instrument (MSI) suggests an increase in burned area and net higher emissions as well as a longer fire season (Roteta et al., 2019; Ramo et al., 2021). Overall, other reasons related to small-scale heterogeneity can explain discrepancies in the modelling of small fire emissions (van Wees & van der Werf, 2019).

5 Summary

We evaluated inverse model calculations of northern tropical African CO_2 fluxes with aircraft measurements over the Atlantic Ocean. This collection of models shows a large

inter-model spread in mean land flux magnitudes and temporal variability in sub-Saharan Africa. The posterior fluxes for NTA averaged over the 2016-2018 period span from -0.2 PgC yr^{-1} to more than 1.8 PgC yr^{-1}. For posterior CO_2 concentrations averaged over optimized ATom boxes, i.e. subregions of the ATom flight transect, the range is around 3 ppm, with a standard deviation between 0.74 and 1 ppm for different campaigns. During the dry season, our ATom emergent constraint indicates that NTA land fluxes are overestimated by the LNLG experiment and underestimated by the IS and OG experiments. Inversion errors could be due to the lack of assimilated in-situ observations in the region, atmospheric transport uncertainties, in particular arising from convection, and the difficulty of achieving accurate and frequent satellite retrievals due to cloud obstruction during the wet season and aerosols during the dry season. The comparison by models, i.e., TM5 or GEOS-Chem, supports the important role of transport biases in the spread of inversions results, which underscores the importance of the Model Intercomparison Project to assess flux estimates. Based on the seasonal timing of the LNLG flux differences, we speculate that the high dust and smoke aerosol loading during the dry season may lead to an overestimated bias correction in the v10 OCO-2 data over NTA. Our results point to the need to better characterize the distribution and impact of biomass burning and dust aerosols to further refine the OCO-2 retrieval or bias correction procedures.

Overall, we found an enhanced seasonal cycle relative to IS inversions, with a larger source during the dry season and a stronger sink during the wet season (Figure S7). Outside of the dry season, the OCO-2 based inversions agree reasonably well with the airborne estimates. The OCO-2 inversions and the ATom-1 and ATom-3 emergent constraints imply a stronger sink during the NTA wet season. Our revised budget for NTA during 2016-2018 is an annual source of 0.14 ± 0.39 PgC yr^{-1}. This is much smaller than the v10 MIP LNLG mean of around 0.9 PgC yr^{-1}.

Past studies and this study suggest the sensitivity of continental scale fluxes to biases in XCO2 in inversions is high, implying the magnitude of remaining biases in OCO-2 data over NTA may be relatively small and challenging to address. Furthermore, given the large spread in total emissions and seasonality of fire emission estimates, the sensitivity of posterior CO_2 to the choice of prior fire flux should be assessed in future studies. Additional constraints on fire fluxes could be obtained by the assimilation of satellite observations of chemical species related to combustion such as CO (Zheng et al., 2018; Gaubert et al., 2020) and nitrogen dioxide (NO_2) and improved burned area estimates (Zheng et al., 2021). For the individual months of the ATom campaigns, we obtain an uncertainty reduction in NTA CO_2 fluxes of a factor of two compared to the full v10 MIP ensemble, highlighting the potential benefit of future airborne observations over and downwind of Africa and other continents. A regular ongoing program of global-scale airborne surveys would greatly improve our ability to resolve the global carbon cycle and validate satellite emission estimates.

Data Availability

The ATom data (Wofsy et al., 2021) is available as 10-sec, NOAA PFP, and Medusa merge products `https://doi.org/10.3334/ORNLDAAC/1925`(10.3334/ORNLDAAC/1925). The OCO-2 v10 MIP model results are publicly available (`https://gml.noaa.gov/ccgg/OCO2_v10mip/`, last accessed 2 March 2023) The NOAA Greenhouse Gas Marine Boundary Layer Reference (Dlugokencky et al., 2019) is publicly available (`https://gml.noaa.gov/ccgg/mbl/data.php`, last accessed 27 December 2022).

References

Adams, A. M., Prospero, J. M., & Zhang, C. (2012). CALIPSO-Derived Three-Dimensional Structure of Aerosol over the Atlantic Basin and Adjacent Continents. *Journal of Climate*, *25*(19), 6862–6879. doi: 10.1175/jcli-d-11-00672.1

Arora, V. K., Katavouta, A., Williams, R. G., Jones, C. D., Brovkin, V., Friedlingstein, P., ... Ziehn, T. (2020). Carbon-concentration and carbon-climate feedbacks in CMIP6 models and their comparison to CMIP5 models. *Biogeosciences*, *17*(16), 4173–4222. doi: 10.5194/bg-17-4173-2020

Barkhordarian, A., Bowman, K. W., Cressie, N., Jewell, J., & Liu, J. (2021). Emergent constraints on tropical atmospheric aridity-carbon feedbacks and the future of carbon sequestration. *Environmental Research Letters*, *16*(11), 114008. doi: 10.1088/1748-9326/ac2ce8

Barkley, A. E., Prospero, J. M., Mahowald, N., Hamilton, D. S., Popendorf, K. J., Oehlert, A. M., ... Gaston, C. J. (2019). African biomass burning is a substantial source of phosphorus deposition to the Amazon, Tropical Atlantic Ocean, and Southern Ocean. *Proceedings of the National Academy of Sciences*, *116*(33), 16216–16221. doi: 10.1073/pnas.1906091116

Basu, S., Baker, D. F., Chevallier, F., Patra, P. K., Liu, J., & Miller, J. B. (2018). The impact of transport model differences on CO_2 surface flux estimates from OCO-2 retrievals of column average CO_2. *Atmospheric Chemistry and Physics*, *18*(10), 7189–7215. doi: 10.5194/acp-18-7189-2018

Bennett, A. C., Dargie, G. C., Cuni-Sanchez, A., Mukendi, J. T., Hubau, W., Mukinzi, J. M., ... Lewis, S. L. (2021). Resistance of african tropical forests to an extreme climate anomaly. *Proceedings of the National Academy of Sciences*, *118*(21), e2003169118. doi: 10.1073/pnas.2003169118

Boggs, P. T., & Rogers, J. E. (1990). Orthogonal distance regression. *Contemporary Mathematics*, *112*, 183–194.

Bowman, K. P. (1993). Large-scale isentropic mixing properties of the Antarctic polar vortex from analyzed winds. *Journal of Geophysical Research*, *98*(D12), 23013. doi: 10.1029/93jd02599

Bowman, K. P., & Carrie, G. D. (2002). The Mean-Meridional Transport Circulation of the Troposphere in an Idealized GCM. *Journal of the Atmospheric Sciences*, *59*(9), 1502–1514. doi: 10.1175/1520-0469(2002)059⟨1502:tmmtco⟩2.0.co;2

Bowman, K. W., Cressie, N., Qu, X., & Hall, A. (2018). A Hierarchical Statistical Framework for Emergent Constraints: Application to Snow-Albedo Feedback. *Geophysical*

Research Letters, *45*(23). doi: 10.1029/2018gl080082

Byrne, B., Baker, D. F., Basu, S., Bertolacci, M., Bowman, K. W., Carroll, D., ... Zeng, N. (2023). National CO_2 budgets (2015–2020) inferred from atmospheric CO_2 observations in support of the global stocktake. *Earth System Science Data*, *15*(2), 963–1004. doi: 10.5194/essd-15-963-2023

Chevallier, F., Bréon, F.-M., & Rayner, P. J. (2007). Contribution of the orbiting carbon observatory to the estimation of co_2 sources and sinks: Theoretical study in a variational data assimilation framework. *Journal of Geophysical Research*, *112*(D9). doi: 10.1029/2006jd007375

Ciais, P., Piao, S.-L., Cadule, P., Friedlingstein, P., & Chédin, A. (2009). Variability and recent trends in the African terrestrial carbon balance. *Biogeosciences*, *6*(9), 1935–1948. doi: 10.5194/bg-6-1935-2009

Connor, B. J., Boesch, H., Toon, G., Sen, B., Miller, C., & Crisp, D. (2008). Orbiting carbon observatory: Inverse method and prospective error analysis. *Journal of Geophysical Research: Atmospheres*, *113*(D5), n/a–n/a. doi: 10.1029/2006jd008336

Cox, P. M. (2019). Emergent constraints on climate-carbon cycle feedbacks. *Current Climate Change Reports*, *5*(4), 275–281. doi: 10.1007/s40641-019-00141-y

Cox, P. M., Pearson, D., Booth, B. B., Friedlingstein, P., Huntingford, C., Jones, C. D., & Luke, C. M. (2013). Sensitivity of tropical carbon to climate change constrained by carbon dioxide variability. *Nature*, *494*(7437), 341–344. doi: 10.1038/nature11882

Crisp, D., Dolman, H., Tanhua, T., McKinley, G. A., Hauck, J., Bastos, A., ... Aich, V. (2022). How Well Do We Understand the Land-Ocean-Atmosphere Carbon Cycle? *Reviews of Geophysics*, *60*(2). doi: 10.1029/2021rg000736

Crounse, J. D., DeCarlo, P. F., Blake, D. R., Emmons, L. K., Campos, T. L., Apel, E. C., ... Wennberg, P. O. (2009). Biomass burning and urban air pollution over the central mexican plateau. *Atmospheric Chemistry and Physics*, *9*(14), 4929–4944. doi: 10.5194/acp-9-4929-2009

Crowell, S., Baker, D., Schuh, A., Basu, S., Jacobson, A. R., Chevallier, F., ... Jones, D. B. A. (2019). The 2015–2016 carbon cycle as seen from OCO-2 and the global in situ network. *Atmospheric Chemistry and Physics*, *19*(15), 9797–9831. doi: 10.5194/acp-19-9797-2019

Curtis, P. G., Slay, C. M., Harris, N. L., Tyukavina, A., & Hansen, M. C. (2018). Classifying drivers of global forest loss. *Science*, *361*(6407), 1108–1111. doi: 10.1126/science.aau3445

Deeter, M. N., Francis, G., Gille, J., Mao, D., Martínez-Alonso, S., Worden, H., ... McKain, K. (2022). The MOPITT Version 9 CO product: sampling enhancements and validation. *Atmospheric Measurement Techniques*, *15*(8), 2325–2344. doi: 10.5194/amt-15-2325-2022

Dlugokencky, E., Thoning, K. W., Lan, X., & Tans, P. P. (2019). *NOAA Greenhouse Gas Reference from Atmospheric Carbon Dioxide Dry Air Mole Fractions from the NOAA GML Carbon Cycle Cooperative Global Air Sampling Network* (Tech. Rep.). National Oceanic and Atmospheric Administration.

Edwards, D. P., Emmons, L. K., Gille, J. C., Chu, A., Attié, J.-L., Giglio, L., ... Drummond, J. R. (2006). Satellite-observed pollution from southern hemisphere biomass burning. *Journal of Geophysical Research*, *111*(D14). doi: 10.1029/2005jd006655

Eldering, A., Wennberg, P. O., Crisp, D., Schimel, D. S., Gunson, M. R., Chatterjee, A., ... Weir, B. (2017, October). The orbiting carbon observatory-2 early science investigations of regional carbon dioxide fluxes. *Science*, *358*(6360), eaam5745. doi: 10.1126/science.aam5745

Evan, A. T., Heidinger, A. K., & Knippertz, P. (2006). Analysis of winter dust activity off the coast of west africa using a new 24-year over-water advanced very high resolution radiometer satellite dust climatology. *Journal of Geophysical Research*, *111*(D12). doi: 10.1029/2005jd006336

Eyring, V., Cox, P. M., Flato, G. M., Gleckler, P. J., Abramowitz, G., Caldwell, P., ... Williamson, M. S. (2019). Taking climate model evaluation to the next level. *Nature*

Climate Change, *9*(2), 102–110. doi: 10.1038/s41558-018-0355-y

Friedlingstein, P., Cadule, P., Piao, S. L., Ciais, P., & Sitch, S. (2010). The african contribution to the global climate-carbon cycle feedback of the 21st century. *Biogeosciences*, *7*(2), 513–519. doi: 10.5194/bg-7-513-2010

Friedlingstein, P., Cox, P., Betts, R., Bopp, L., von Bloh, W., Brovkin, V., ... Zeng, N. (2006). Climate-Carbon Cycle Feedback Analysis: Results from the C4MIP Model Intercomparison. *Journal of Climate*, *19*(14), 3337–3353. doi: 10.1175/jcli3800.1

Friedlingstein, P., Jones, M. W., O'Sullivan, M., Andrew, R. M., Bakker, D. C. E., Hauck, J., ... Zeng, J. (2022). Global Carbon Budget. *Earth System Science Data*, *14*(4), 1917–2005. doi: 10.5194/essd-14-1917-2022

Gaubert, B., Emmons, L. K., Raeder, K., Tilmes, S., Miyazaki, K., Jr., A. F. A., ... Diskin, G. S. (2020). Correcting model biases of CO in East Asia: impact on oxidant distributions during KORUS-AQ. *Atmospheric Chemistry and Physics*, *20*(23), 14617–14647. doi: 10.5194/acp-20-14617-2020

Gaubert, B., Stephens, B. B., Basu, S., Chevallier, F., Deng, F., Kort, E. A., ... Yin, Y. (2019). Global atmospheric CO_2 inverse models converging on neutral tropical land exchange, but disagreeing on fossil fuel and atmospheric growth rate. *Biogeosciences*, *16*(1), 117–134. doi: 10.5194/bg-16-117-2019

Gonzalez, Y., Commane, R., Manninen, E., Daube, B. C., Schiferl, L. D., McManus, J. B., ... Wofsy, S. C. (2021). Impact of stratospheric air and surface emissions on tropospheric nitrous oxide during ATom. *Atmospheric Chemistry and Physics*, *21*(14), 11113–11132. doi: 10.5194/acp-21-11113-2021

Gurney, K., & Denning, A. (2008). *TransCom 3: Annual Mean CO2 Flux Estimates from Atmospheric Inversions (Level 1)*. ORNL Distributed Active Archive Center. doi: 10.3334/ORNLDAAC/895

Gurney, K., Law, R. M., Denning, A. S., Rayner, P. J., Baker, D., Bousquet, P., ... Yuen, C.-W. (2002, February). Towards robust regional estimates of CO_2 sources and sinks using atmospheric transport models. *Nature*, *415*(6872), 626–630. doi: 10.1038/415626a

Hong, C., Burney, J. A., Pongratz, J., Nabel, J. E. M. S., Mueller, N. D., Jackson, R. B., & Davis, S. J. (2021). Global and regional drivers of land-use emissions in 1961-2017. *Nature*, *589*(7843), 554–561. doi: 10.1038/s41586-020-03138-y

Houweling, S., Baker, D., Basu, S., Boesch, H., Butz, A., Chevallier, F., ... Zhuravlev, R. (2015). An intercomparison of inverse models for estimating sources and sinks of CO2 using GOSAT measurements. *Journal of Geophysical Research: Atmospheres*, *120*(10), 5253–5266. doi: 10.1002/2014jd022962

Ichoku, C., Ellison, L. T., Yue, Y., Wang, J., & Kaiser, J. W. (2016). Fire and smoke remote sensing and modeling uncertainties. In *Natural hazard uncertainty assessment* (pp. 215–230). John Wiley & Sons, Inc. doi: 10.1002/9781119028116.ch14

Kaminski, T., Scholze, M., Vossbeck, M., Knorr, W., Buchwitz, M., & Reuter, M. (2017). Constraining a terrestrial biosphere model with remotely sensed atmospheric carbon dioxide. *Remote Sensing of Environment*, *203*, 109–124. doi: 10.1016/j.rse.2017.08.017

Keenan, T. F., Luo, X., Kauwe, M. G. D., Medlyn, B. E., Prentice, I. C., Stocker, B. D., ... Zhou, S. (2021). a constraint on historic growth in global photosynthesis due to increasing CO2. *Nature*, *600*(7888), 253–258. doi: 10.1038/s41586-021-04096-9

Kiel, M., O'Dell, C. W., Fisher, B., Eldering, A., Nassar, R., MacDonald, C. G., & Wennberg, P. O. (2019). How bias correction goes wrong: measurement of affected by erroneous surface pressure estimates. *Atmospheric Measurement Techniques*, *12*(4), 2241–2259. doi: 10.5194/amt-12-2241-2019

Lewis, S. L., Lopez-Gonzalez, G., Sonké, B., Affum-Baffoe, K., Baker, T. R., Ojo, L. O., ... Wöll, H. (2009). Increasing carbon storage in intact African tropical forests. *Nature*, *457*(7232), 1003–1006. doi: 10.1038/nature07771

Li, Q., Jacob, D. J., Yantosca, R. M., Heald, C. L., Singh, H. B., Koike, M., ... Streets, D. G. (2003). A global three-dimensional model analysis of the atmospheric budgets

of HCN and CH3cn: Constraints from aircraft and ground measurements. *Journal of Geophysical Research: Atmospheres*, *108*(D21). doi: 10.1029/2002jd003075

Liu, J., Bowman, K. W., Schimel, D. S., Parazoo, N. C., Jiang, Z., Lee, M., . . . Eldering, A. (2017, October). Contrasting carbon cycle responses of the tropical continents to the 2015–2016 el niño. *Science*, *358*(6360), eaam5690. doi: 10.1126/science.aam5690

Liu, T., Mickley, L. J., Marlier, M. E., DeFries, R. S., Khan, M. F., Latif, M. T., & Karambelas, A. (2020). Diagnosing spatial biases and uncertainties in global fire emissions inventories: Indonesia as regional case study. *Remote Sensing of Environment*, *237*, 111557. doi: 10.1016/j.rse.2019.111557

Long, M. C., Stephens, B. B., McKain, K., Sweeney, C., Keeling, R. F., Kort, E. A., . . . Wofsy, S. C. (2021). Strong southern ocean carbon uptake evident in airborne observations. *Science*, *374*(6572), 1275–1280. doi: 10.1126/science.abi4355

Masarie, K. A., Peters, W., Jacobson, A. R., & Tans, P. P. (2014). ObsPack: a framework for the preparation, delivery, and attribution of atmospheric greenhouse gas measurements. *Earth Syst. Sci. Data*, *6*(2), 375–384. doi: 10.5194/essd-6-375-2014

Nelson, R. R., & O'Dell, C. W. (2019). The impact of improved aerosol priors on near-infrared measurements of carbon dioxide. *Atmospheric Measurement Techniques*, *12*(3), 1495–1512. doi: 10.5194/amt-12-1495-2019

Nguyen, H. M., & Wooster, M. J. (2020). Advances in the estimation of high spatio-temporal resolution pan-african top-down biomass burning emissions made using geostationary fire radiative power (FRP) and MAIAC aerosol optical depth (AOD) data. *Remote Sensing of Environment*, *248*, 111971. doi: 10.1016/j.rse.2020.111971

O'Dell, C. W., Eldering, A., Wennberg, P. O., Crisp, D., Gunson, M. R., Fisher, B., . . . Velazco, V. A. (2018, December). Improved retrievals of carbon dioxide from Orbiting Carbon Observatory-2 with the version 8 ACOS algorithm. *Atmospheric Measurement Techniques*, *11*(12), 6539-6576. doi: 10.5194/amt-11-6539-2018

Ott, L., Pawson, S., & Bacmeister, J. (2011). An analysis of the impact of convective parameter sensitivity on simulated global atmospheric CO distributions. *Journal of Geophysical Research: Atmospheres*, *116*(D21). doi: 10.1029/2011jd016077

Palmer, P. I., Feng, L., Baker, D., Chevallier, F., Bösch, H., & Somkuti, P. (2019). Net carbon emissions from african biosphere dominate pan-tropical atmospheric co_2 signal. *Nature Communications*, *10*(1), 3344. doi: 10.1038/s41467-019-11097-w

Pan, Y., Birdsey, R. A., Fang, J., Houghton, R., Kauppi, P. E., Kurz, W. A., . . . Hayes, D. (2011). A large and persistent carbon sink in the world's forests. *Science*, *333*(6045), 988–993. doi: 10.1126/science.1201609

Peiro, H., Crowell, S., Schuh, A., Baker, D. F., O'Dell, C., Jacobson, A. R., . . . Baker, I. (2022). Four years of global carbon cycle observed from the orbiting carbon observatory 2 (OCO-2) version 9 and in situ data and comparison to OCO-2 version 7. *Atmospheric Chemistry and Physics*, *22*(2), 1097–1130. doi: 10.5194/acp-22-1097-2022

Philip, S., Johnson, M. S., Baker, D. F., Basu, S., Tiwari, Y. K., Indira, N. K., . . . Poulter, B. (2022). OCO-2 satellite-imposed constraints on terrestrial biospheric co_2 fluxes over south asia. *Journal of Geophysical Research: Atmospheres*, *127*(3). doi: 10.1029/2021jd035035

Philip, S., Johnson, M. S., Potter, C., Genovesse, V., Baker, D. F., Haynes, K. D., . . . Poulter, B. (2019). Prior biosphere model impact on global terrestrial co_2 fluxes estimated from OCO-2 retrievals. *Atmospheric Chemistry and Physics*, *19*(20), 13267–13287. doi: 10.5194/acp-19-13267-2019

Prospero, J. M. (1999). Long-range transport of mineral dust in the global atmosphere: Impact of african dust on the environment of the southeastern united states. *Proceedings of the National Academy of Sciences*, *96*(7), 3396–3403. doi: 10.1073/pnas.96.7.3396

Ramo, R., Roteta, E., Bistinas, I., van Wees, D., Bastarrika, A., Chuvieco, E., & van der Werf, G. R. (2021). African burned area and fire carbon emissions are strongly impacted by small fires undetected by coarse resolution satellite data. *Proceedings of the National Academy of Sciences*, *118*(9), e2011160118. doi: 10.1073/pnas.2011160118

Randerson, J. T., Chen, Y., van der Werf, G. R., Rogers, B. M., & Morton, D. C. (2012).

Global burned area and biomass burning emissions from small fires. *Journal of Geophysical Research: Biogeosciences*, *117*(G4), n/a–n/a. doi: 10.1029/2012jg002128

Ray, E. (2022). *Atom: Back trajectories and influences of air parcels along flight track, 2016-2018.* ORNL Distributed Active Archive Center. doi: 10.3334/ORNLDAAC/1889

Renoult, M., Annan, J. D., Hargreaves, J. C., Sagoo, N., Flynn, C., Kapsch, M.-L., . . . Mauritsen, T. (2020). A bayesian framework for emergent constraints: case studies of climate sensitivity with PMIP. *Climate of the Past*, *16*(5), 1715–1735. doi: 10.5194/cp-16-1715-2020

Roberts, G., Wooster, M. J., & Lagoudakis, E. (2009). Annual and diurnal african biomass burning temporal dynamics. *Biogeosciences*, *6*(5), 849–866. doi: 10.5194/bg-6-849-2009

Rodríguez, S., Cuevas, E., Prospero, J. M., Alastuey, A., Querol, X., López-Solano, J., . . . Alonso-Pérez, S. (2015). Modulation of saharan dust export by the north african dipole. *Atmospheric Chemistry and Physics*, *15*(13), 7471–7486. doi: 10.5194/acp-15-7471-2015

Roteta, E., Bastarrika, A., Padilla, M., Storm, T., & Chuvieco, E. (2019). Development of a sentinel-2 burned area algorithm: Generation of a small fire database for sub-saharan africa. *Remote Sensing of Environment*, *222*, 1–17. doi: 10.1016/j.rse.2018.12.011

Sanderson, B. M., Pendergrass, A. G., Koven, C. D., Brient, F., Booth, B. B. B., Fisher, R. A., & Knutti, R. (2021). The potential for structural errors in emergent constraints. *Earth System Dynamics*, *12*(3), 899–918. doi: 10.5194/esd-12-899-2021

Santoni, G. W., Daube, B. C., Kort, E. A., Jiménez, R., Park, S., Pittman, J. V., . . . Wofsy, S. C. (2014). Evaluation of the airborne quantum cascade laser spectrometer (QCLS) measurements of the carbon and greenhouse gas suite – CO_2, CH_4, N_2O, and CO – during the CalNex and HIPPO campaigns. *Atmospheric Measurement Techniques*, *7*(6), 1509–1526. doi: 10.5194/amt-7-1509-2014

Schimel, D., Stephens, B. B., & Fisher, J. B. (2015, December). Effect of increasing co_2 on the terrestrial carbon cycle. *Proceedings of the National Academy of Sciences*, *112*(2), 436–441. doi: https://doi.org/10.1073/pnas.1407302112

Schuh, A. E., Byrne, B., Jacobson, A. R., Crowell, S. M. R., Deng, F., Baker, D. F., . . . Weir, B. (2022). On the role of atmospheric model transport uncertainty in estimating the Chinese land carbon sink. *Nature*, *603*(7901), E13–E14. doi: 10.1038/s41586-021-04258-9

Schuh, A. E., Jacobson, A. R., Basu, S., Weir, B., Baker, D., Bowman, K., . . . Palmer, P. I. (2019). Quantifying the impact of atmospheric transport uncertainty on CO 2 surface flux estimates. *Global Biogeochemical Cycles*, *33*(4), 484–500. doi: 10.1029/2018gb006086

Simpson, I. R., McKinnon, K. A., Davenport, F. V., Tingley, M., Lehner, F., Fahad, A. A., & Chen, D. (2021). Emergent constraints on the large scale atmospheric circulation and regional hydroclimate: do they still work in CMIP6 and how much can they actually constrain the future? *Journal of Climate*, *34*, 6355–6377. doi: 10.1175/jcli-d-21-0055.1

Stephens, B. B., Gurney, K. R., Tans, P. P., Sweeney, C., Peters, W., Bruhwiler, L., . . . Denning, A. S. (2007). Weak northern and strong tropical land carbon uptake from vertical profiles of atmospheric co_2. *Science*, *316*(5832), 1732–1735. doi: 10.1126/science.1137004

Stephens, B. B., Morgan, E. J., Bent, J. D., Keeling, R. F., Watt, A. S., Shertz, S. R., & Daube, B. C. (2021). Airborne measurements of oxygen concentration from the surface to the lower stratosphere and pole to pole. *Atmospheric Measurement Techniques*, *14*(3), 2543–2574. doi: 10.5194/amt-14-2543-2021

Sweeney, C., Karion, A., Wolter, S., Newberger, T., Guenther, D., Higgs, J. A., . . . Tans, P. P. (2015). Seasonal climatology of CO_2 across north america from aircraft measurements in the NOAA/ESRL global greenhouse gas reference network. *Journal of Geophysical Research: Atmospheres*, *120*(10), 5155–5190. doi: 10.1002/2014jd022591

Taylor, T. E., O'Dell, C. W., Baker, D., Bruegge, C., Chang, A., Chapsky, L., . . . Zong,

J. (2023). Evaluating the consistency between OCO-2 and OCO-3 XCOsub2/sub estimates derived from the NASA ACOS version 10 retrieval algorithm. *Atmos. Meas. Tech. Discuss. [preprint]*. doi: 10.5194/amt-2022-329

Thompson, C. R., Wofsy, S. C., Prather, M. J., Newman, P. A., Hanisco, T. F., Ryerson, T. B., ... Zeng, L. (2022). The NASA Atmospheric Tomography (ATom) Mission: Imaging the Chemistry of the Global Atmosphere. *Bulletin of the American Meteorological Society*, *103*(3), E761–E790. doi: 10.1175/bams-d-20-0315.1

Thoning, K. W., Tans, P. P., & Komhyr, W. D. (1989). Atmospheric carbon dioxide at Mauna Loa Observatory: 2. Analysis of the NOAA GMCC data, 1974-1985. *Journal of Geophysical Research: Atmospheres*, *94*(D6), 8549–8565. doi: 10.1029/jd094id06p08549

Valentini, R., Arneth, A., Bombelli, A., Castaldi, S., Gatti, R. C., Chevallier, F., ... Scholes, R. J. (2014). A full greenhouse gases budget of Africa: synthesis, uncertainties, and vulnerabilities. *Biogeosciences*, *11*(2), 381–407. doi: 10.5194/bg-11-381-2014

van der Werf, G. R., Randerson, J. T., Giglio, L., van Leeuwen, T. T., Chen, Y., Rogers, B. M., ... Kasibhatla, P. S. (2017). Global fire emissions estimates during 1997–2016. *Earth System Science Data*, *9*(2), 697–720. doi: 10.5194/essd-9-697-2017

van Wees, D., & van der Werf, G. R. (2019). Modelling biomass burning emissions and the effect of spatial resolution: a case study for africa based on the global fire emissions database (GFED). *Geoscientific Model Development*, *12*(11), 4681–4703. doi: 10 .5194/gmd-12-4681-2019

Wang, X., Piao, S., Ciais, P., Friedlingstein, P., Myneni, R. B., Cox, P., ... Chen, A. (2014). A two-fold increase of carbon cycle sensitivity to tropical temperature variations. *Nature*, *506*(7487), 212–215. doi: 10.1038/nature12915

Wigneron, J.-P., Fan, L., Ciais, P., Bastos, A., Brandt, M., Chave, J., ... Fensholt, R. (2020). Tropical forests did not recover from the strong 2015–2016 el niño event. *Science Advances*, *6*(6). doi: 10.1126/sciadv.aay4603

Williamson, D. B., & Sansom, P. G. (2019). How Are Emergent Constraints Quantifying Uncertainty and What Do They Leave Behind? *Bulletin of the American Meteorological Society*, *100*(12), 2571–2588. doi: 10.1175/bams-d-19-0131.1

Williamson, M. S., Thackeray, C. W., Cox, P. M., Hall, A., Huntingford, C., & Nijsse, F. J. (2021). Emergent constraints on climate sensitivities. *Reviews of Modern Physics*, *93*(2), 025004. doi: 10.1103/revmodphys.93.025004

Wofsy, S., Afshar, S., Allen, H., Apel, E., Asher, E., Barletta, B., ... Vieznor, N. (2021). *Atom: Merged atmospheric chemistry, trace gases, and aerosols, version 2.* ORNL Distributed Active Archive Center. doi: 10.3334/ORNLDAAC/1925

Zheng, B., Chevallier, F., Ciais, P., Yin, Y., Deeter, M. N., Worden, H. M., ... He, K. (2018). Rapid decline in carbon monoxide emissions and export from East Asia between years 2005 and 2016. *Environmental Research Letters*, *13*(4), 044007. doi: 10.1088/1748 -9326/aab2b3

Zheng, B., Ciais, P., Chevallier, F., Chuvieco, E., Chen, Y., & Yang, H. (2021). Increasing forest fire emissions despite the decline in global burned area. *Science Advances*, *7*(39). doi: 10.1126/sciadv.abh2646